AFRL-AFOSR-UK-TR-2023-0032

Experimental study of turbulent flow over permeable rough surfaces

Ganapathisubramani, Bharathram
UNIVERSITY OF SOUTHAMPTON
UNIVERSITY ROAD
SOUTHAMPTON, , SO17 1BJ
GBR

12/13/2022
Final Technical Report

Air Force Research Laboratory
Air Force Office of Scientific Research
European Office of Aerospace Research and Development
Unit 4515 Box 14, APO AE 09421

REPORT DOCUMENTATION PAGE

PLEASE DO NOT RETURN YOUR FORM TO THE ABOVE ORGANIZATION.

1. REPORT DATE	2. REPORT TYPE	3. DATES COVERED	
20221213	Final	START DATE 20190701	END DATE 20220630

4. TITLE AND SUBTITLE
Experimental study of turbulent flow over permeable rough surfaces

5a. CONTRACT NUMBER	5b. GRANT NUMBER	5c. PROGRAM ELEMENT NUMBER
	FA9550-19-1-7022	
5d. PROJECT NUMBER	**5e. TASK NUMBER**	**5f. WORK UNIT NUMBER**

6. AUTHOR(S)
Bharathram Ganapathisubramani

7. PERFORMING ORGANIZATION NAME(S) AND ADDRESS(ES)
UNIVERSITY OF SOUTHAMPTON
UNIVERSITY ROAD
SOUTHAMPTON SO17 1BJ
GBR

8. PERFORMING ORGANIZATION REPORT NUMBER

9. SPONSORING/MONITORING AGENCY NAME(S) AND ADDRESS(ES)	10. SPONSOR/MONITOR'S ACRONYM(S)	11. SPONSOR/MONITOR'S REPORT NUMBER(S)
EOARD UNIT 4515 APO AE 09421-4515	AFRL/AFOSR IOE	AFRL-AFOSR-UK-TR-2023-0032

12. DISTRIBUTION/AVAILABILITY STATEMENT
A Distribution Unlimited: PB Public Release

13. SUPPLEMENTARY NOTES

14. ABSTRACT
A variety of turbulent flows are over surface that are rough and permeable. Evolution, engineering design, manufacturing constraints and natural phenomena lead to rough and permeable boundaries in these porous surfaces (e.g. flow in heat exchangers, forest and urban canopies, bird feathers and river beds). The permeability and the roughness of a porous surface alters the turbulent boundary layer that develops over it and consequently the wake past an object with surface porosity. This entirely depends on the interaction between the external flow in the boundary layer over the roughness or the wake and the flow field within the porous media. Despite the wide-ranging impact and relevance, there is a clear lack of fundamental understanding and the scaling laws that relate the properties of porous media to the features of external flow. In this project, we carried out a systematic study where we explored the coupling between roughness and porosity and their effects on turbulent boundary layer flows.We performed systematic wind tunnel experiments over permeable and rough surfaces in order to examine if the flow over such surfaces can be considered in the same framework as flow over rough surfaces. Data indicates that this is indeed possible and that we might be able to define a sand grain roughness associated with permeability and another that is associated with roughness. Together, these two definitions can be combined to make predictions on the drag incurred by preamble rough surfaces. We also examined the influence of permeability and roughness on the flow structure within the boundary layer. The combination of permeability and roughness have very counterinuititive effects on the flow structure.

15. SUBJECT TERMS

16. SECURITY CLASSIFICATION OF:			17. LIMITATION OF ABSTRACT	18. NUMBER OF PAGES
a. REPORT	b. ABSTRACT	c. THIS PAGE	SAR	21
U	U	U		

19a. NAME OF RESPONSIBLE PERSON	19b. PHONE NUMBER *(Include area code)*
DOUGLAS SMITH	314 235 6013

Experimental study of turbulent flow over permeable rough surfaces

Final Report for FA9550-19-1-7022

PI: B. Ganapathisubramani

Participants
Martin Sanchez Romero
Dea Daniella Wangsawijaya
Prateek Jaiswal

Aeronautical and Astronautical Engineering,
University of Southampton SO17 1BJ, United Kingdom

1 Introduction

Flow over porous walls comprise an extensive number of natural phenomena, ranging from blood vessels to the atmospheric boundary layer (ABL) developing over a forest canopy. The latter can be considered as a turbulent boundary layer (TBL) developing over a porous wall. An example of porous walls, constructed from packed spheres, is shown in figure 1. Here, both walls approximately have the same permeability (resistance of a substrate to fluid flow), but the wall shown in figure 1(a) has a roughness interface above the porous wall, while in figure 1(b) this interface comprises of a flat surface. Thus, a realistic representation of a porous wall is *both* permeable *and* rough to some extent: for the wall in figure 1(a), the effects of both permeability and roughness have to be considered for characterisation of a TBL developing over such wall, while for figure 1(b), the roughness effect may be negligible.

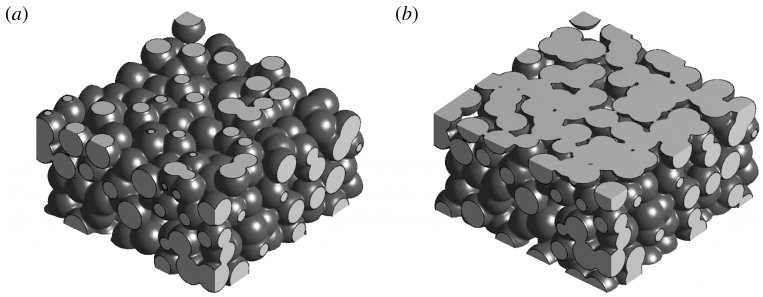

Figure 1: Illustrations of realistic permeable walls with: (a) a rough wall on the interface and (b) flat interface. Adapted from Rosti *et al.* (2015).

1.1 Rough walls

TBLs developing over rough walls are relatively well characterised. The presence of rough walls increases skin friction from that of smooth walls and thus its time-averaged streamwise velocity U can be written as a downward shift of the logarithmic region ΔU^+ from the smooth wall velocity profile

$$U^+ = \frac{1}{\kappa}\ln\left[\frac{(y+y_0)U_\tau}{\nu}\right] + B - \Delta U^+ = \frac{1}{\kappa}\ln(y+y_0)^+ + B - \Delta U^+ \tag{1}$$

The viscous-scaled velocity is defined as $U^+ \equiv U/U_\tau$, where $U_\tau \equiv \sqrt{\tau_w/\rho}$ is the friction velocity, τ_w and ρ are the wall shear stress (WSS) and the density of fluid, respectively. The logarithmic profile is defined as follows: κ is the von Kármán constant, y_0 is the zero-plane displacement, ν is the kinematic viscosity of fluid, and B is the log-law intercept. The logarithmic shift ΔU^+, also known as the Hama roughness function (Hama, 1954), is defined as

$$\Delta U^+ = \frac{1}{\kappa}\ln\left(\frac{k_s U_\tau}{\nu}\right) + B - B_{FR} = \frac{1}{\kappa}\ln k_s^+ + B - B_{FR} \tag{2}$$

where k_s is the equivalent sand grain roughness and $B_{FR} = 8.5$ is the 'fully' rough intercept of the velocity profile of sand grain roughness. This is a roughness parameterisation suggested by Nikuradse (1933); k_s is a measure of roughness effect on the flow relative to that of a uniform sand grain roughness (as opposed to a measure of physical roughness), and it can only be determined by flow measurements. The mean streamwise velocity profile of a rough wall can therefore be written as a function of its k_s

$$U^+ = \frac{1}{\kappa} \ln\left(\frac{y + y_0}{k_s}\right) + B_{FR} \tag{3}$$

1.2 Permeable walls

While the characterisation of rough wall TBLs are relatively well-defined by the Hama roughness function, the characterisation of permeable wall is less so. Earlier studies of permeable walls involved various types of such walls, namely: packed spheres (Zagni & Smith, 1976), perforated sheets (Kong & Schetz, 1982), bed of grains (Zippe & Graf, 1983), and multi-layered walls (Manes *et al.*, 2009). In these studies, permeable walls increase drag (i.e. skin friction coefficient $C_f \equiv 2(U_\tau/U_\infty)^2$) from that of solid, impermeable walls, which is attributed to the increase of dissipation (Zagni & Smith, 1976), momentum flux, and Reynolds shear stress (Shimizu *et al.*, 1990) on the interface between the fluid and the porous substrates. Similar to the rough wall TBLs, the increase in C_f of permeable walls is also characterised by a downward shift in the logarithmic region from that of a solid, smooth wall (Hahn *et al.*, 2002; Efstathiou & Luhar, 2018). Thus, it is probable that there is a "universal" parameter that characterise permeable walls – possibly similar to k_s for rough wall TBLs. Several candidates have been investigated in previous studies for characterisation of permeable walls. Breugem *et al.* (2006) highlighted three lengthscales that define an isotropic permeable wall: permeability K, wall thickness k, and the size of element comprising the porous substrate d_p. In order to fully isolate the effect of permeability on the flow, it was further suggested by Breugem *et al.* (2006) that these conditions, related to the three lengthscales, have to be met: (i) the wall has to be thicker than the flow penetration depth into the substrate, (ii) the Reynolds number based on the substrate size, defined by $Re_{d_p} \equiv d_p U_\tau/\nu$, has to be small (note that $Re_{d_p} < 5$ for a hydrodynamically smooth wall, Nikuradse, 1933), and (iii) the Reynolds number based on permeability $Re_K \equiv \sqrt{K} U_\tau/\nu$ has to be high ($Re_K > 1$). It was further suggested by Manes *et al.* (2011) that the logarithmic region of a TBL developing over a permeable wall scales on permeability K in the following manner

$$U^+ = \frac{1}{\kappa} \ln\left(\frac{y + y_0}{\sqrt{K}}\right) + c_1 \tag{4}$$

Equation (4) can be rearrange to show a downward logarithmic shift, equivalent to that of rough wall boundary layers

$$U^+ = \frac{1}{\kappa} \ln(y + y_0)^+ - \frac{1}{\kappa} \ln Re_K + c_1 \tag{5}$$

Various magnitude of the von Kármán constant κ has been observed: $\kappa = 0.23$ (Breugem *et al.*, 2006), $0.31 \leq \kappa \leq 0.33$ (Manes *et al.*, 2011), and κ as a function of Re_K (Suga *et al.*, 2010). This variety is largely attributed to the low Reynolds number in which these studies were conducted and thus there was not enough separation between the inner and outer layers of the wall-bounded flows (Manes *et al.*, 2011). A more recent experimental work by Esteban *et al.* (2022), conducted at a higher order of magnitude of Reynolds number ($2000 \leq Re_\tau \leq 18000$), observed that $\kappa = 0.39$, similar to that of smooth and rough wall TBLs ($\kappa \approx 0.4$). It was further hypothesised by Esteban *et al.* (2022) that c_1 in equation (5) is an additive constant related to the blockage effect of a porous substrate, as a realistic permeable wall comprises of both porous matrix and solid substrates (see, for example, figure 1), whose size does not permit the full isolation of permeability effect, $Re_{d_p} < 5$ (Breugem *et al.*, 2006). This blockage effect might be represented by a roughness function, similar to ΔU^+ in equation (2)

$$U^+ = \frac{1}{\kappa}\ln(y + y_0)^+ - \frac{1}{\kappa}\ln Re_K - \Delta U_b^+ + B \tag{6}$$

$$U^+ = \frac{1}{\kappa}\ln(y + y_0)^+ - \frac{1}{\kappa}\ln Re_K - \frac{1}{\kappa}\ln k_{s_b}^+ + B_{FR} \tag{7}$$

$$U^+ = \frac{1}{\kappa}\ln\left(\frac{y + y_0}{Re_K k_{s_b}}\right) + B_{FR} \tag{8}$$

where subscript 'b' denote the blockage effect of the porous substrate. By comparing equation (3) and (8), the 'equivalent sand grain roughness' k_s of a porous wall can be defined as

$$k_{s_p} = Re_K k_{s_b} \tag{9}$$

The similarities between the effects of roughness and permeability on the TBLs developing over such surfaces suggest the possibility of characterising porous wall using the same framework for rough wall TBLs. Equation (9) further suggests the possibility of decoupling the effects of permeability (denoted by Re_K) and blockage from the porous substrate (k_{s_b}) when a porous wall is considered. This formulation represents the porous wall in figure 1(b). For the porous wall in figure 1(a), however, an additional roughness effect (from the roughness interface above the porous wall) has to be considered as well. Question remains as to whether this additional roughness effect conforms to that of equation (9) or whether an additional roughness term, similar the to log-law shift due to rough walls in equation (5), has to be introduced. In terms of turbulent structures, the near-wall cycles in smooth wall TBLs are replaced by coherent roughness element-sized structures (Castro, 2007) in the presence of rough walls, while permeability weakens these near-wall structures Breugem *et al.* (2006); Rosti *et al.* (2015). Flow penetration into a porous wall has been observed to alter the dynamics of coherent structure formation above the wall (Manes *et al.*, 2011; Fang *et al.*, 2018). Thus, in this study we aim to: (i) characterise porous walls (akin to figure 1b) and a combination of porous-rough walls (akin to figure 1a) using the framework previously used for rough wall TBLs, (ii) decouple the effect of permeability and roughness in the porous-rough walls combination, and (iii) examine the turbulent structures formed by porous-rough walls, both near-wall and the large-scale structures.

In this study, measurements are conducted in TBLs developing over various test surfaces: porous, rough, and porous-rough wall combinations. Measurements are conducted inside a boundary layer wind tunnel at a constant streamwise location while varying U_∞/ν. This allows a wide range of Re_τ ($11000 \leq Re_\tau \leq 32000$), ensuring an extended logarithmic region and enough separation between inner and outer layers of the TBLs. The test surfaces are comprised of a commercially available foam sheet as the porous wall, two types of rough walls, and combinations of these walls (porous wall topped with either of the rough walls). Only one type of porous wall is tested over a range of Re_τ, ensuring a set of matched Re_τ and permeability effect Re_K for each combination of porous, rough, and porous-rough, while the two types of rough walls allow a systematic variation of roughness effect. Hot-wire anemometry (HWA) measures the streamwise velocity component as a function of time and wall-normal location. The porous wall allows flow penetration into its porous matrix, but we are unable to conduct flow measurements inside this matrix as the HWA measurements only reach the top of the wall. Thus, we conduct wall-pressure fluctuation measurements simultaneously with HWA measurements, in order to obtain the full picture of the TBLs. The streamwise velocity of a developing TBL can be decomposed into its Reynolds (temporal) average U, and the fluctuation about their temporal average u' and

$$u(\boldsymbol{x}, t) = U(\boldsymbol{x}) + u'(\boldsymbol{x}, t) \tag{10}$$

where the axis system $\boldsymbol{x} = (x, y, z)$ corresponds to the streamwise, wall-normal, and spanwise directions, respectively. The wall-pressure fluctuation is denoted by $p'(x, 0, z, t)$.

2 Experimental Setup

2.1 Facility

Measurements are conducted inside the closed return boundary layer wind tunnel (BLWT) at the University of Southampton. The flow passes through a contraction section of 6:1 ratio before entering the 12 m × 1.2 m × 1 m (length × width × height) test section. The boundary layer develops over the floor (bottom surface) of the BLWT, where various test surfaces (figure 3) are installed. A 200 mm-long smooth wall ramp is installed at the end of the contraction section (figure 2(a)) to match the thickness of the test surfaces. This ramp marks the inlet towards the test section of the BLWT and the streamwise datum ($x = 0$). The boundary layer is tripped by a 8.5 mm-wide, 0.4 mm-thick plastic zig-zag turbulator tape attached on the ramp (figure 2(b)). The tunnel has the freestream turbulence level of $\sigma_{u'}/U_\infty \approx 0.1\%$, where $\sigma_{u'}$ is the standard deviation of streamwise turbulent fluctuation at the freestream and U_∞ is the freestream velocity. The BLWT is equipped with a water-cooled heat exchanger, maintaining the flow temperature variation of 1.32% for the longest measurements (~8 hours).

The roof (top surface) of the BLWT is non-adjustable. Thus, the measurements for all test surfaces are conducted in nominally favourable pressure gradients, as indicated by the magnitude of the wake parameter Π of the wake function of the mean velocity profile of Coles (1956), $2\Pi/\kappa W(y/\delta)$. For all test surfaces, $\Pi = 0.29 \pm 0.17$ for all

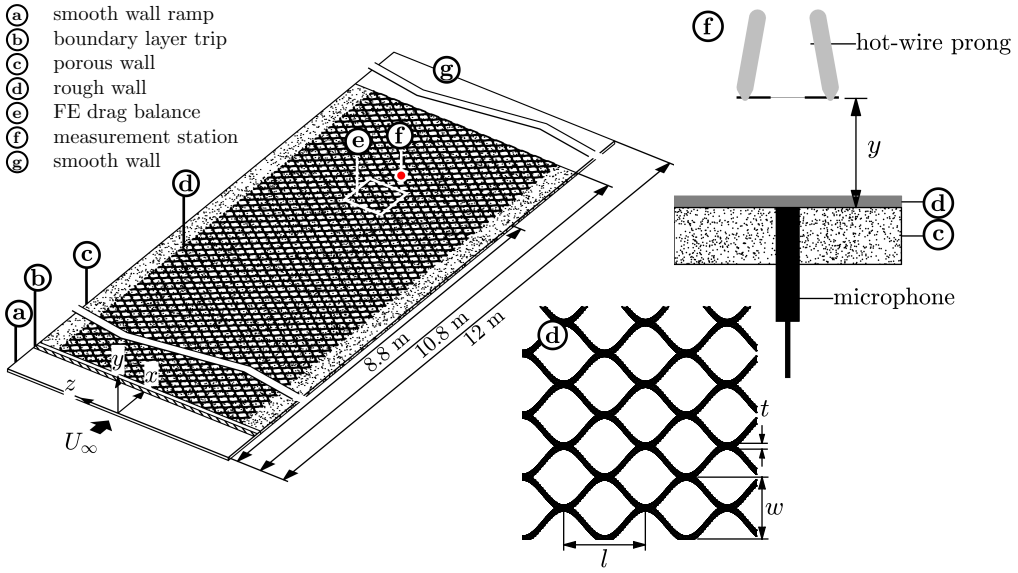

Figure 2: Illustration of a porous-rough surface laid inside the test section of the boundary layer wind tunnel. Inset ⓕ: simultaneous hot-wire anemometry and wall pressure fluctuation measurements at the measurement station (not to scale). y is the wall-normal distance between the wire sensor and the wall (measured from the surface of the porous/solid wall); the microphone is flush-mounted on the surface of the porous/smooth wall. Inset ⓓ: geometric parameters of the metal mesh (rough wall), where l is the length of the longway of the mesh, w is the length of the shortway of the mesh, and t is the width of the mesh strand. See table 1 for details.

test surfaces (table 2), which is less than that of zero pressure gradient TBLs, $\Pi \approx 0.4$ (Chauhan *et al.*, 2009; Marusic *et al.*, 2015). Π is estimated by fitting the obtained velocity profile to the composite profile of Rodríguez-López *et al.* (2015).

2.2 Test surfaces

Six test surfaces are constructed for this study: the baseline smooth wall ('**S**'), porous wall (denoted by '**P**', figure 3a), two types of rough walls (denoted by '**R1**' and '**R2**', figure 3b–c), and two types of porous-rough walls (denoted by '**PR1**' and '**PR2**', figure 3d–e). All test surfaces are assembled on the bottom surface of the BLWT, downstream of the ramp and trip (figure 2), with the smooth wall covering the test section up to $x = 12$ m. The ramp with either porous, rough, or porous-rough walls only cover the first 10.8 m-long part of the test section, while the section from $x = 10.8$ m to $x = 12$ m comprises of a smooth surface (figure 2). All measurements are conducted at $x = 8.8$ m from the datum of the tunnel test section (figure 2ⓕ), slightly downstream of a floating element (FE) drag balance located at $x = 8.6$ m (figure 2ⓔ). To obtain a wide range of Reynolds number (Re), the freestream velocity is varied

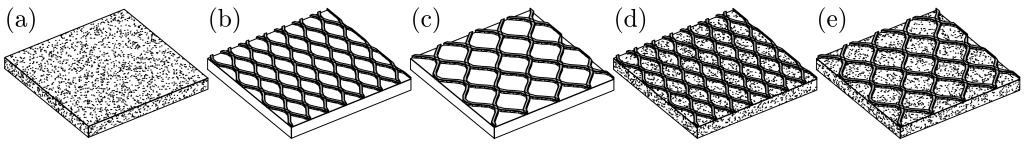

Figure 3: Illustrations of all test surfaces in the present study: (a) porous wall **P**, rough walls (b) **R1** and (c) **R2**, porous-rough walls (d) **PR1** and (e) **PR2**.

Surface	k [mm]	s [mm]	ε [–]	K [$\times 10^{-8}$ m^2]	A_o [–]	l [mm]	w [mm]	t [mm]
P	15	0.89	0.859	3.62	–	–	–	–
R1	3.0	–	–	–	0.73	62	30	4
R2	3.5	–	–	–	0.81	70	53	5

Table 1: Geometric parameters of the porous **P** and rough walls **R1** and **R2**, where k is the thickness of the foam and metal meshes. For **P**: s is the average pore size of the foam, ε is the porosity, and K is the permeability. For **R1** and **R2**: A_o is the open area ratio of the mesh, while the definitions of l, w, and t are illustrated in figure 2 (see inset ⓓ).

between $U_\infty \approx 12$ to 40 ms^{-1}, corresponding to the unit Re of $U_\infty/\nu \approx 8 \times 10^5$ to 2.67×10^6 m^{-1}, respectively. Details of all measurements are summarised in table 2.

The porous walls are constructed from sheets of 15 mm-thick ($700 \leq k^+ \equiv kU_\tau/\nu \leq 2130$), 45 ppi (pores per inch) polyurethane reticulated foam, as illustrated in figure 3(a). The porous substrate has the porosity (the ratio of empty volume to total volume) of $\varepsilon = 0.859$ and the average pore size of $s = 0.89$ mm ($41 \leq s^+ \equiv sU_\tau/\nu \leq 126$), as analysed by Esteban *et al.* (2022) from CT-scan data of the same porous substrate. The permeability is $K = 3.62 \times 10^{-8}$ m^2, measured by a 'Darcy'-type experiment (Esteban *et al.*, 2022) and corresponding to the Reynolds number based on permeability $9 \leq Re_K \equiv \sqrt{K}U_\tau/\nu \leq 27$. The ramp and porous walls cover the first 10.8 m-long and the entire 1.2 m-wide ($x \times z$) working section of the BLWT (figure 2). Details of the relevant parameters regarding the porous substrate is given in table 1.

The rough walls are constructed from a smooth surface topped with either of the two types of expanded metal mesh sheets denoted by **R1** and **R2**, as illustrated in figure 3(b,c). The mesh sheets alone have the thickness of $k = 3$ and 3.5 mm for **R1** and **R2**, respectively, which approximately corresponds to $140 \leq k^+ \leq 497$. The mesh patterns are produced by cutting slits into a metal sheet, which is then expanded to obtain the desired mesh size. **R1** (figure 3b) has a diamond-shaped mesh with an open area A_o (ratio of empty to total area in xz–plane) of 0.73, while **R2** (figure 3c) has a square-shaped mesh with $A_o = 0.81$. Details of the mesh geometries, including the length and width of each mesh, as well as the thickness of each mesh strand are given in table 1 and illustrated in figure 2ⓓ. Due to the limited availability of wider metal sheets from the manufacturer, both mesh sheets only cover a 1 m-wide portion (in z) of

Case	δ [mm]	θ [mm]	U_∞ [ms^{-1}]	U_τ [ms^{-1}]	Re_x [$\times 10^7$]	Re_θ [$\times 10^4$]	Re_τ [$\times 10^4$]	Re_K [–]	C_f [$\times 10^{-3}$]	Π [–]	ΔU^+ [–]	k_s [mm]	k_s^+ [–]	Sym.
Smooth walls														
S	122.21	11.96	39.51	1.30	2.32	3.15	1.06	–	2.18	0.32	–	–	–	□
Porous walls														
P*	199.01	24.03	15.21	0.82	0.92	2.50	1.11	10.63	5.75	0.30	11.38	7.83	437	○
P*	201.11	24.55	19.84	1.06	1.18	3.29	1.44	13.62	5.72	0.27	12.01	7.83	560	○
P*	199.96	24.45	25.45	1.36	1.52	4.21	1.85	17.57	5.74	0.27	12.66	7.83	723	○
P*	208.26	25.37	29.06	1.54	1.76	5.07	2.21	20.22	5.65	0.31	13.02	7.83	832	○
P*	211.27	25.88	35.46	1.87	2.14	6.30	2.72	24.50	5.59	0.34	13.52	7.83	1008	○
P*	221.25	26.43	40.05	2.13	2.39	7.18	3.20	27.52	5.67	0.24	13.81	7.83	1132	○
Rough walls														
R1	232.40	26.24	14.90	0.75	0.87	2.79	1.16	–	5.12	0.32	10.64	6.47	323	△
R1	236.84	28.57	19.93	1.00	1.17	3.80	1.58	–	5.01	0.32	11.38	6.47	430	△
R1	239.38	28.45	25.20	1.28	1.48	4.78	2.03	–	5.12	0.33	12.00	6.47	549	△
R1	243.78	28.60	29.58	1.50	1.73	5.63	2.43	–	5.14	0.31	12.42	6.47	645	△
R1	254.33	29.34	35.21	1.77	2.05	6.38	2.97	–	5.04	0.34	12.82	6.47	756	△
R1	243.76	29.09	39.79	2.01	2.32	7.65	3.23	–	5.08	0.33	13.14	6.47	857	△
R2	241.11	29.16	15.10	0.73	0.89	2.93	1.18	–	4.70	0.46	10.34	5.89	287	◇
R2	229.33	28.30	19.74	0.97	1.15	3.71	1.48	–	4.85	0.38	11.07	5.89	381	◇
R2	229.34	27.99	24.90	1.23	1.46	4.64	1.88	–	4.89	0.38	11.68	5.89	483	◇
R2	230.03	28.41	29.83	1.46	1.75	5.65	2.24	–	4.81	0.42	12.12	5.89	575	◇
Porous-rough walls														
PR1	216.77	26.49	12.43	0.70	0.73	2.20	1.02	8.95	6.43	0.23	11.98	11.67	549	☆
PR1*	225.41	26.70	17.28	1.00	1.01	3.06	1.49	12.55	6.65	0.13	12.85	11.67	770	☆
PR1	218.12	27.05	21.47	1.22	1.26	3.89	1.78	15.50	6.43	0.22	13.39	11.67	951	☆
PR1*	227.93	27.13	26.04	1.50	1.54	4.76	2.30	19.17	6.61	0.16	13.93	11.67	1176	☆
PR1*	226.64	27.20	31.49	1.77	1.85	5.71	2.68	22.53	6.35	0.24	14.35	11.67	1382	☆
PR1*	229.11	27.05	35.01	2.01	2.05	6.30	3.07	25.52	6.63	0.12	14.67	11.67	1565	☆
PR2*	219.42	27.03	15.06	0.80	0.90	2.76	1.20	10.37	5.68	0.31	11.65	8.74	477	☆
PR2*	221.73	27.19	19.97	1.07	1.20	3.72	1.63	14.02	5.79	0.27	12.42	8.74	644	☆
PR2*	224.41	27.37	25.20	1.35	1.52	4.73	2.08	17.60	5.73	0.29	13.00	8.74	809	☆
PR2*	222.96	27.81	28.26	1.50	1.69	5.35	2.28	19.48	5.66	0.28	13.26	8.74	895	☆

Table 2: Summary of all test surfaces: baseline smooth walls (**S**), porous (**P**), rough (**R1** and **R2**), and porous-rough (**PR1** and **PR2**) walls. The statistics are obtained from HWA measurements: δ is the 99% boundary-layer thickness and θ is the momentum thickness. Reynolds number definitions are: $Re_x \equiv xU_\infty/\nu$, $Re_\theta \equiv \theta U_\infty/\nu$, $Re_\tau \equiv \delta U_\tau/\nu$, and $Re_K \equiv \sqrt{K}U_\tau/\nu$. Coefficient of friction is defined as $C_f \equiv 2(U_\tau/U_\infty)^2$. The last column shows the symbol associated with each test surface. Colours denote test cases with approximately matched $Re_\tau \approx 11300$ (○), 15200 (○), 19200 (○), 22900 (○), 27900 (○), and 31700 (○). Asterisks ('*') with the same colours in the first column denote cases with matched Re_K.

the working section of the BLWT, leaving a 100-mm gap on the left and right hand side edges of this section (figure 2).

Two types of porous-rough walls are constructed from the porous wall topped with metal meshes: **PR1** (figure 3d) from the 45-ppi porous sheets topped with **R1** (metal mesh sheets with 73% open area) and **PR2** (figure 3e) from the same porous sheets topped with **R2** (81% open area mesh sheets). For analysis and decoupling of porous and rough walls effects on the turbulent flows, present study is conducted within a range of matched friction Reynolds number $Re_\tau \equiv \delta U_\tau/\nu$ (here, δ is the 99% boundary-layer thickness) between **P**, **R1**, and **PR1**, as well as another set of matched Re_τ for **P**, **R2**, and **PR2**. The first set of test surfaces constructed from **R1** has six cases of matched $Re_\tau \approx$ 11300, 15200, 19200, 22900, 27900, and, 31700 while the second set constructed from **R2** has four matched cases of $Re_\tau \approx$ 11300, 15200, 19200, and 22900. It should be noted that these Re_τ are the averages of test surfaces with *approximately* similar Re_τ, within the maximum range of $Re_\tau \pm 1500$. For comparisons, two baseline smooth wall cases (**S**) are included in this study (table 2). As the maximum flow speed of the BLWT is $U_\infty \approx 50$ ms^{-1} and the measurements are conducted at constant x, we are only able to match the smooth walls with the lowest $Re_\tau \approx 11300$. Details of each test surfaces, including the statistics obtained from HWA and WSS measurements, are given in table 2. Throughout this study, each test surface is denoted with a specific symbol (see the last column in table 2); however, the same colour denotes surfaces with matched Re_τ, which runs from lighter towards darker colour as Re_τ increases.

2.3 Simultaneous velocity–wall pressure fluctuation measurements

Hot-wire anemometry (HWA) measurements are conducted for all test surfaces listed in table 2. Measurements of the streamwise velocity component u of the turbulent boundary layer developing over each test surface are carried out by traversing the wire in wall-normal direction y across 35–40 logarithmically-spaced points from the wall towards the freestream of the BLWT. Here, the datum $y = 0$ is located at the upper surface of the smooth wall for cases **S**, **R1**, and **R2**, and at the upper surface of the porous wall for cases **P**, **PR1**, and **PR2** (figure 2ⓕ). All measurements are conducted at $x = 8.8$ m from the start of the test section and at the centreline of the BLWT (in z), to ensure minimum effects of secondary vortices arising from the gaps between the side walls of the BLWT and the rough walls (figure 2).

Measurements are carried out using a modified Dantec 55P05 single-sensor, boundary-layer type probe attached to a Dantec 55H21 probe support. The sensor is manufactured by soldering a 5 µm diameter tungsten wire to the tip of the hot-wire prong, which is then coated with copper, leaving a 1-mm long portion of the wire exposed (figure 2ⓕ). This sensor length l_w satisfies the recommended wire length-to-diameter ratio of 200 (Ligrani & Bradshaw, 1987) and corresponds to the viscous-scaled lengths of $47 \leq l_w^+ \equiv l_w U_\tau/\nu \leq 142$. The sensor is connected to a Dantec Streamline Pro Constant Temperature Anemometer (CTA), which has the overheat ratio of 0.8. The output signal is sampled from the CTA at $f_s = 30$ kHz, yielding viscous-scaled sampling interval of $1.1 \leq t^+ \equiv U_\tau^2/(f_s\nu) \leq 10$. The sampling time T_s at each measurement point differs between test surfaces such that the boundary-layer turnover time is maintained at $T_s U_\infty/\delta \geq 20000$ to allow convergence of turbulence energy spectra (Hutchins

et al., 2009). The sensor is traversed to the freestream and calibrated prior to and after each measurement. The relation between freestream velocity U_∞ and output voltage of the sensor E_∞ is defined by King's law $E_\infty^2 = C_1 + C_2 U_\infty^{C_3}$, whose constants C_n are obtained by curve fitting the calibration data. Temperature compensation is applied to the output signal to account for a slight sensor drift. Ambient temperature is measured by an RTD TST414 thermometer located at the inlet of the BLWT working section, while atmospheric pressure is measured by a Setra 278 barometric pressure transducer (air density ρ is calculated by assuming perfect gas relation, while kinematic viscosity ν using Sutherland's law). Freestream velocity is calculated using a Pitot-static tube (connected to a Furness FCO560 manometer) located at the freestream of the measurement station. Signals are digitised with a 16-bit NI-USB 6212 data acquisition (DAQ) board and controlled via MATLAB.

Wall pressure fluctuation p' measurements are conducted simultaneously with HWA measurements using a GRAS PH40 CCP free-field array microphone (S/N 33950), which is flush-mounted on the upper surface of the porous wall for cases **P**, **PR1**, and **PR2** (figure 2ⓕ), whilst ensuring that the diaphragm is not covered by the mesh sheets. The microphone is mounted below the hot-wire probe, its centreline approximately coincides with the wire sensor. Signals are acquired simultaneously with those of the hot-wire as the wire is traversed in y towards the freestream. The diaphragm has the diameter d of 6.35 mm ($296 \leq d^+ \equiv dU_\tau/\nu \leq 902$), with frequency response roll-off at ~10 kHz. Sensitivity of the microphone is measured using a GRAS 42AB sound calibrator (114 dB at 1 kHz), corresponding to the magnitude of 48.69 mV/Pa. For cases **R1** and **R2**, a different GRAS PH40 microphone is used (S/N 314275). This microphone is flush-mounted on the upper surface of the smooth wall, below the mesh sheets. Calibration with GRAS 42AB sound calibrator results in the sensitivity of 34.43 mV/Pa. It should be noted that the simultaneous p' measurements are not conducted for the baseline smooth wall cases.

2.4 Wall shear stress (WSS) measurements

The wall shear stresses (WSSs) of all test surfaces shown in table 2 are measured using an in-house floating element (FE) drag balance. The balance has a 200 mm × 200 mm FE located at $x = 8.6$ m (figure 2ⓔ), upstream of the HWA measurement station. A section of each test surfaces are cut according to the size of the FE and mounted on top of the FE, leaving a 0.5 mm clearance between the FE and its housing, allowing it to move freely for WSS measurements. The housing is sealed to prevent airflow into the balance. Measurements are acquired at $f_s = 256$ Hz with 120 s sampling time for each test surface. Calibration of the balance is performed before measurements by loading a set of calibration weights to the balance via a pulley system. The relationship between known mass m and time-averaged output voltage E from the balance is obtained by fitting the calibration data into a first order polynomial, $m = aE$ (figure 4a). Error bars in figure 4(a) denote the uncertainties in E measurements, $E \pm 0.96\%$ (maximum). Calibrations are performed within the range of 0 g (unloaded balance) to 16 g for the smooth walls, and 0 to 45 g for the rest of the test surfaces due to the increase in C_f for these surfaces. The WSS τ_w is proportional to the force mg (where g is the gravitational acceleration). Due to the nominally favourable pressure gradient of the

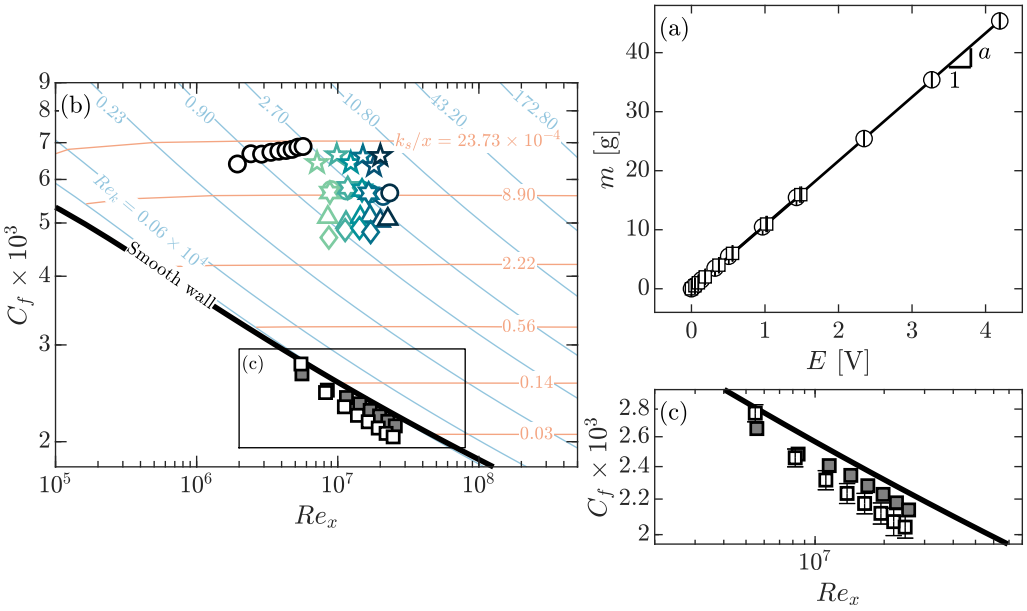

Figure 4: (a) Floating element drag balance calibration curve: mass of the calibration weights m as a function of time-averaged output voltage E for smooth (□) and porous walls (○). Solid lines are $m = aE$. (b) Coefficient of friction C_f as a function of Re_x for all test surfaces, including the smooth walls, obtained from WSS measurements with FE drag balance (□) and fitted to the composite profile of Rodríguez-López *et al.* (2015) (■). Details of measurement uncertainties shown in (c). For comparison, C_f of the same porous surface (○), obtained by Esteban *et al.* (2022) are shown. Solid lines denote the C_f of the following: smooth wall (——), porous wall (k_s = 7.83 mm) obtained at constant $Re_k \equiv kU_\infty/\nu$ (——), and porous wall at constant k_s/x (——), obtained from the method proposed in Monty *et al.* (2016). Legends are shown in table 2.

developing TBL in the BLWT (see §2.1), the measured force mg is corrected for non-zero pressure gradient $\mathrm{d}p/\mathrm{d}x$ measured by two static pressure taps attached upstream and downstream of the FE, respectively.

Figure 4(b) shows the coefficient of frictions of all tests surfaces $C_f \equiv 2(U_\tau/U_\infty)^2$ as a function of fetch Reynolds number $Re_x \equiv xU_\infty/\nu$. The C_f of the baseline smooth wall cases are determined using three different methods: (i) direct WSS measurements using the FE drag balance (□), (ii) fitting velocity profiles obtained from HWA measurements to the composite profile of Rodríguez-López *et al.* (2015) (■), (iii) an analytical solution described by Monty *et al.* (2016) (——), which show a reasonable agreement with each other. It should be noted that for baseline smooth wall cases, HWA and WSS measurements are conducted within a range of U_∞, $10 \lesssim U_\infty \lesssim 45$ ms^{-1}. However, only one of these cases has matched Re_τ with those of **P**, **R**, and **PR** cases; the rest are not shown in table 2 for brevity. Figur 4(c) shows the details of C_f measurements of the smooth wall. Error bars are the uncertainties of FE drag balance measurements, $C_f \pm 3.67\%$ (maximum). The measured smooth wall C_f is compared against that obtained by composite profile fittings and the analytical solution, with the maximum difference of 4.95% and 6.05% , respectively.

For the rest of the test surfaces **P**, **R**, and **PR**, C_f are determined from direct WSS measurements. For the porous wall, C_f of the same porous substrate, measured in a different facility (Esteban *et al.*, 2022) is shown in '○' symbol in figure 4(a) for comparison. Both rough walls (**R1** and **R2**) have lower C_f than that of porous walls, but the porous-rough walls (**PR1** and **PR2**) increase the C_f from that of rough walls, as shown in figure 4(a).

3 Results

3.1 Flow statistics

Figure 5(a) shows the inner-scaled mean streamwise velocity U^+ as a function of y^+ for test surfaces **P**, **R1**, and **PR1** for matched Re_τ (table 2). A vertical downward shift in the logarithmic and wake regions from the smooth wall profile is observed for the aforementioned test surfaces (note that we are only able to match the smooth wall with the lowest Re case, $Re_\tau \approx 11300$). The logarithmic region of all porous and rough surfaces collapses with equation (1), and the smooth wall with $1/\kappa(y + y_0)^+ + B$. For these test surfaces, $\kappa = 0.39$ and the log-law intercept $B = 4.32 \pm 0.03$ (porous and rough surfaces) and $B = 4.35 \pm 0.01$ (smooth walls), obtained from the modified fitting method of Rodríguez-López *et al.* (2015). It is noted that $\kappa = 0.39$ is consistent with that obtained for TBLs developing over various polyurethane foam walls measured by Esteban *et al.* (2022) over a range of lower magnitude of Re, $2000 \leq Re_\tau \leq 18000$. Permeability effect is apparent in the porous walls (**P**), with the mean velocity reaches an asymptote of $U^+ \approx 5$ closer to the walls. The effect of roughness (added blockage) is further apparent in **PR1**, where the asymptote drops further to $U^+ \approx 3$. Similar phenomena, i.e. the log-law characterised by $\kappa = 0.39$ and $B \approx 4.3$, as well as permeability effect closer to the wall are also observed for the other rough walls (**R2** and **PR2**) in figure 5(b). For **PR2** surfaces, the asymptote denoting permeability effect

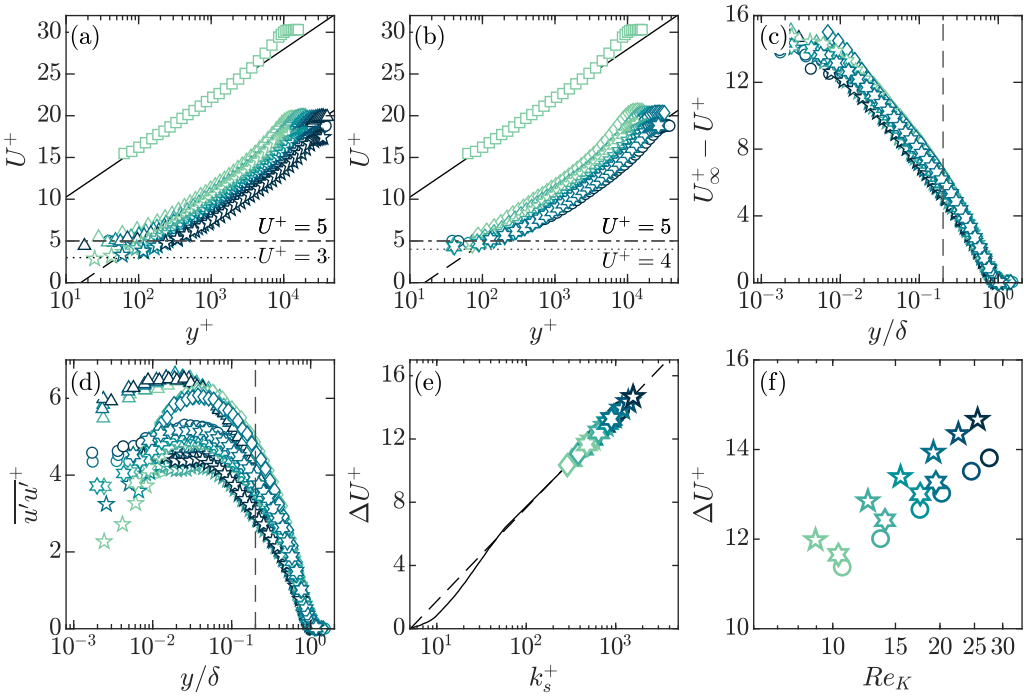

Figure 5: Flow statistics obtained from HWA measurements: (a,b) mean streamwise velocity $U^+ \equiv U/U_\tau$, (c) mean streamwise velocity defect $U_\infty^+ - U^+$, and (d) the variance of streamwise velocity fluctuation $\overline{u'u'}^+$ for all test surfaces: (a) **P**, **R1**, and **PR1**, (b) **P**, **R2**, and **PR2**. In (a,b), ——: $1/\kappa \ln y^+ + B$, where $\kappa = 0.39$ and $B \approx 4.3$; - - -: $1/\kappa \ln y^+ + B - \Delta U^+$. In (c,d), - - -: $y/\delta = 0.2$. (e) Log-law shift ΔU^+ as a function of equivalent sand grain roughness k_s^+. Solid line (——) is obtained by Nikuradse (1933) and dashed line (- - -) is $1/\kappa \ln k_s^+ + B - B_{FR}$. (f) ΔU^+ as a function of Re_K for **P**, **PR1**, and **PR2**. Legends are shown in table 2.

occurs at $U^+ \approx 4$, which is consistent with the lower C_f for this roughness (**R2**) compared to that of **R1** (figure 4a). Although the measurements are conducted under nominally favourable pressure gradient condition, the outer layer similarity is largely preserved at $y/\delta \geq 0.2$, as shown in the velocity defect profile in figure 5(c).

For parameterisation of the surfaces, the mean flow profiles obtained from HWA measurements are fitted to the modified composite profile of Rodríguez-López *et al.* (2015), in which the log-law shift term ΔU^+ is added, forming equation (1). The equivalent sand grain 'roughness' k_s is obtained from the fitted ΔU^+ for all test surfaces via equation (2). It should be noted, however, that the 'k_s' obtained from the fitted ΔU^+ here captures the roughness effect for **R1** and **R2** (equation 2), permeability and blockage effects of the porous substrate **P** (equation 6–8), and all of these effects for **PR1** and **PR2**. Figure 5(e) shows the log-law shift ΔU^+ as a function of k_s^+. All test surfaces collapse to the logarithmic function $1/\kappa \ln k_s^+ + B - B_{FR}$ (equation 2), although this is given since k_s is not obtained independently from ΔU^+. The magnitude of k_s^+ (table 2) exceeds the threshold defined by Flack & Schultz (2010), $k_s^+ \gtrsim 70$, ensuring that all test surfaces are 'fully' rough and thus ΔU^+ depends solely on k_s.

Figure 4(b) also shows C_f vs. Re_x for 'rough' walls, solved analytically by Monty *et al.* (2016) given that Re_x is varied in two different manners: either (i) maintaining constant unit $Re, U_\infty/\nu$ (solid blue line), or (ii) maintaining constant fetch length x (solid red line). Present study is conducted in the latter manner. The analytical solutions of C_f vs. Re_x, plotted in either constant $Re_k \equiv kU_\tau/\nu$ or constant k_s/x, are shown here for the porous walls, where $k = 15$ mm and $k_s = 7.83$ mm. For the same porous substrate (**P**) in the present study, conducted at $k_s/x = 8.9 \times 10^{-4}$ ($k_s = 7.83$ mm), as well as a previous study by Esteban *et al.* (2022) at higher order of $k_s/x = 2.4 \times 10^{-3}$ ($k_s = 7.97$ mm), the directly measured C_f is in good agreement with its analytical solution.

The effect of permeability is shown in figure 5(f) for test surfaces comprises of porous walls: **P**, **PR1**, and **PR2**, where the log-law shift ΔU^+ is plotted as a function of Re based on permeability, Re_K. It should be noted that ΔU^+ here accounts for the total momentum deficit (from that of smooth wall TBLs) in both porous and porous-rough walls. Although it is clear that the momentum deficit is logarithmically scaled by Re_K, universality, as shown in figure 5(e) with k_s, is not apparent. This highlights the importance of accounting for the 'blockage' effect, as well as permeability in a porous substrate (equation 6–8). Further analysis to obtain the blockage term (especially when roughness is added on top of a porous wall in case **PR1** and **PR2**) and decoupling of permeability and roughness effects will be discussed in detail in §3.3.

3.2 Energy spectra

Figures 6 and 7 show the 1-D energy spectra of the streamwise velocity fluctuation $\Phi_{u'u'}$, calculated from the HWA signals acquired at each wall-normal locations y. The spectra is presented in premultiplied form, whose relationship with the variance of streamwise fluctuation is given by

$$\overline{u'u'} = \int_0^\infty f\Phi_{u'u'}\mathrm{d}(\ln f) \tag{11}$$

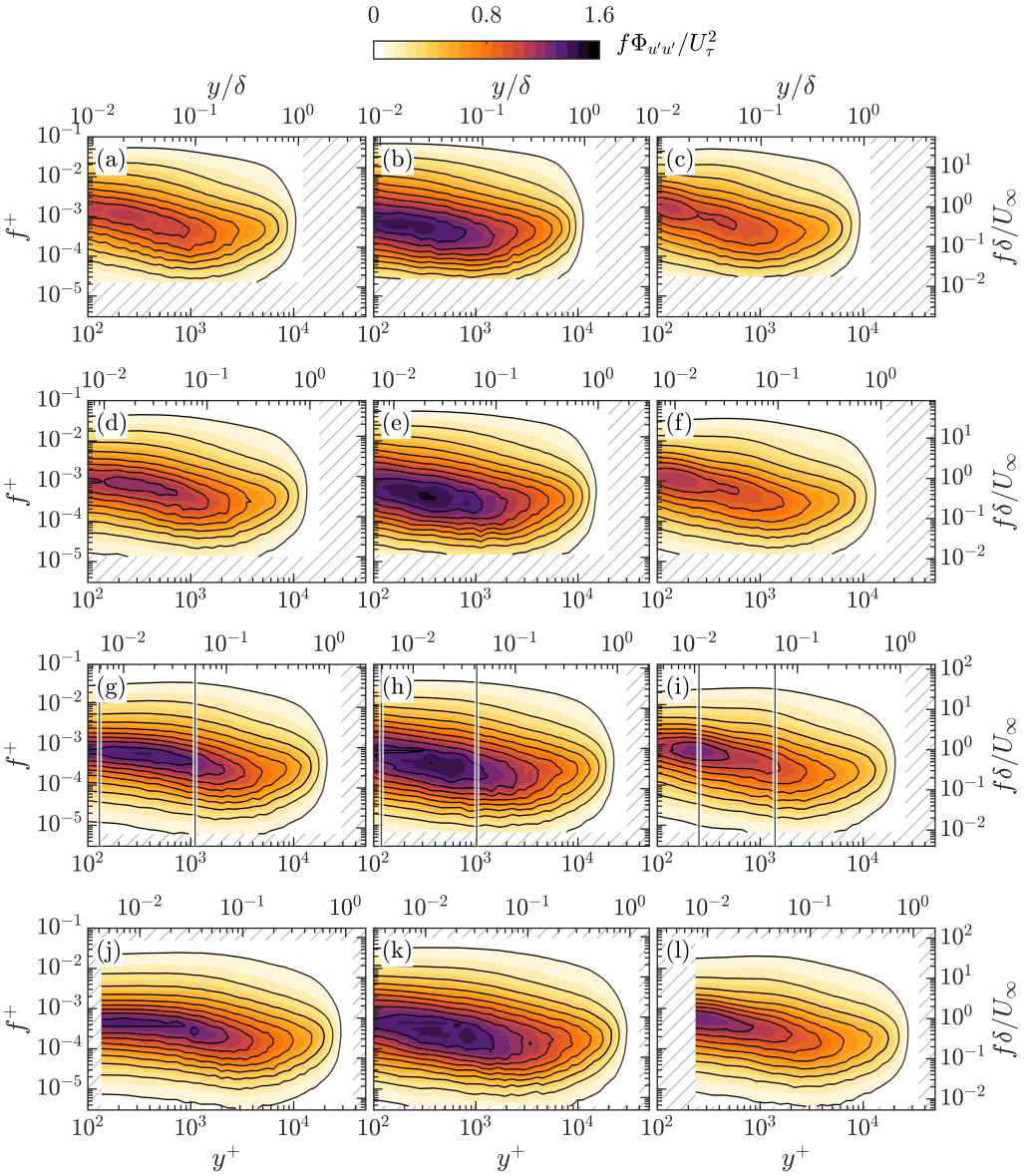

Figure 6: Contours of (inner-scaled) permultiplied 1-D streamwise energy spectra $f\Phi_{u'u'}/U_\tau^2$ as a function of frequency $f^+ \equiv f\nu/U_\tau^2$ and wall-normal location $y^+ \equiv yU_\tau/\nu$ of: (a,d,g,j) porous wall (**P**), (b,e,h,k) rough wall (**R1**) and (c,f,i,l) porous-rough wall (**PR1**). Cases with matched Re_τ are shown in the same column: (a–c) $Re_\tau \approx 11300$, (d–f) 15200, (g–i) 22900, and (j–l) 31700. In (g–i), solid lines (——) are the wall-normal locations from which the energy spectra is extracted and shown in figure 8. Outer-scaled axis ($f\delta/U_\infty$ and y/δ) are available at the right ordinate and top abscissa. Data are not available in the hatched regions.

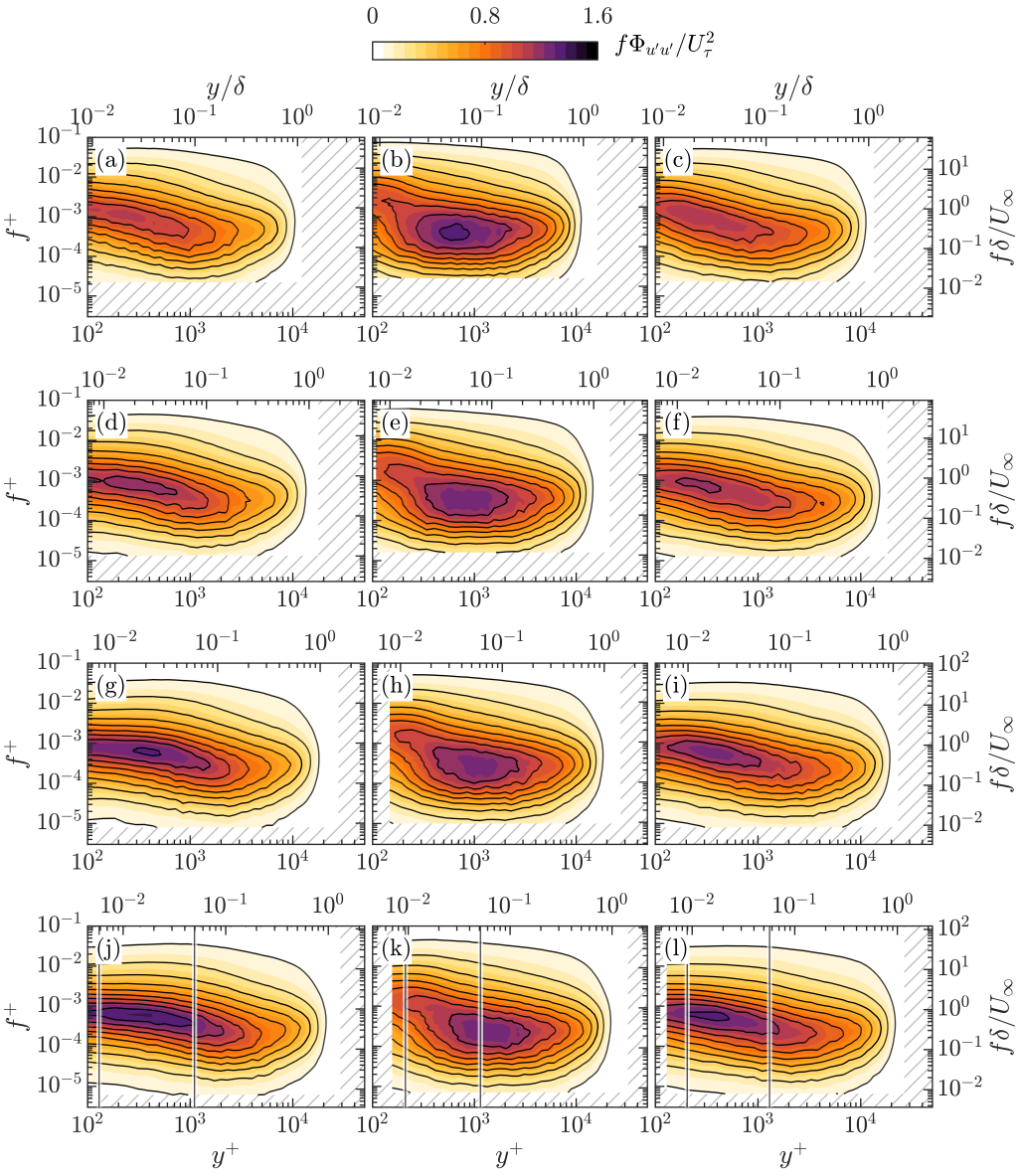

Figure 7: Contours of (inner-scaled) permultiplied 1-D streamwise energy spectra $f\Phi_{u'u'}/U_\tau^2$ as a function of f^+ and wall-normal location z^+ of: (a,d,g,j) porous wall (**P**), (b,e,h,k) rough wall (**R2**) and (c,f,i,l) porous-rough wall (**PR2**). Cases with matched Re_τ are shown in the same column: (a–c) $Re_\tau \approx 11300$, (d–f) 15200, (g–i) 19200, and (j–l) 22900. In (j–l), solid lines (——) are the wall-normal locations from which the energy spectra is extracted and shown in figure 8. Outer-scaled axis are available at the right ordinate and top abscissa. Data are not available in the hatched regions.

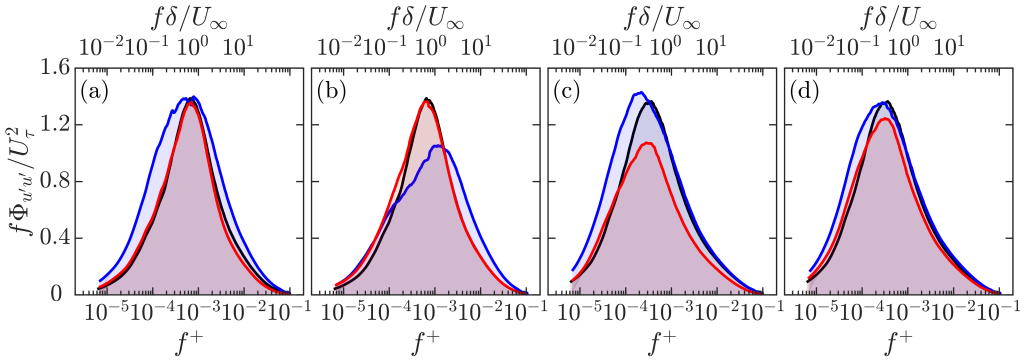

Figure 8: Contours of permultiplied 1-D streamwise energy spectra $f\Phi_{u'u'}/U_\tau^2$ as a function of f^+ at the wall-normal location y with same convection velocities (a,b) $U/U_\infty = 0.3$ and (c,d) $U/U_\infty = 0.5$ for porous-rough test surfaces (**PR**, $Re_\tau \approx 22900$) with surfaces (a,c) **R1** and (b,d) **R2** as the roughness. ——: ——: **P**, ——: **R**, ——: **PR**.

where f is the frequency of a given Fourier mode. Contours of $f\Phi_{u'u'}$ is normalised by U_τ^2 and presented as a function of the inner-scaled wall-normal location y^+ and $f^+ \equiv f\nu/U_\tau^2$. Outer-scaled axis (y/δ and $f\delta/U_\infty$, respectively) are presented at the right hand side ordinate and top abscissa. Figures are shown for selected matched Re_τ cases for **PR1** and all matched Re_τ for **R2**. Cases with matched Re_τ are shown in the same row, while the three columns, from left to right, denote the porous, rough, and porous-rough test surfaces.

The turbulent energy distribution of TBLs developing over porous, rough, and porous-rough surfaces are presented by comparing the 1-D spectrograms of the aforementioned surfaces at certain wall-normal locations. As these surfaces have different drag (figure 4a) and therefore different convection velocity $U(y)$ at the same y, here the comparisons are presented at wall-normal locations that share the same U/U_∞. Two wall-normal locations are chosen, representing region near the wall ($U/U_\infty = 0.3$) and within the logarithmic region ($U/U_\infty = 0.5$). These locations are marked by solid lines in figure 6(g–i) and 7(j–l) for a matched $Re_\tau \approx 22900$.

Figure 8(a) shows the 1-D premultiplied energy spectra $f\Phi_{u'u'}/U_\tau^2$ for test surfaces **P** (——), **R1** (——), and **PR1** (——) at the same convection velocity $U/U_\infty = 0.3$, which corresponds to the wall-normal location $y^+ \approx 100$, 100, and 250 for these surfaces. The premultiplied energy spectra of surfaces **P** and **R1** collapses, signalling similar turbulent energy distribution at this convection velocity, while the energy is distributed within a wider range of frequency above the rough wall **R1**. The energy spectra peaks at approximately the same frequency. A different behaviour at the same convection velocity $U/U_\infty = 0.3$ for the other set of porous-rough walls **R2** and **PR2** in figure 8(b). Here, peak of energy spectra of the rough wall **R2** is shifted towards higher frequency range (associated with smaller turbulent scales). The energy distribution in **PR2** is affected by the presence of the rough wall **R2**, especially in the lower frequency

range (i.e. larger scales), where the spectra of both walls collapses. In higher frequency, however, the spectra of **PR2** reverts to that of porous wall **P**. It should be noted that the HWA measurements are conducted locally above the roughness open area and this might be the reason for closer energy distribution between **PR** and **P**, compared to **R**.

Figure 8(c,d) shows the spectra $f\Phi_{u'u'}/U_\tau^2$ at matched convection velocity $U/U_\infty = 0.5$, which corresponds to the wall-normal locations inside the logarithmic region, $0.04 \lesssim y/\delta \lesssim 0.06$. Figure 8(c) shows that the spectra of **PR1** collapses at lower frequency with the porous wall **P**, but at higher frequency only **P** and **R1** collapse together. Meanwhile, the spectra of other porous-roughness combination: **P**, **R2**, and **PR2** in figure 8(d) show a reasonable collapse at both lower and higher frequencies, signalling an approach towards outer layer similarity.

3.3 Decoupling permeability and roughness effect

It is assumed that the presence of roughness over the porous wall increase the logarithmic shift further by

$$U^+ = \frac{1}{\kappa}\ln(y+y_0)^+ - \frac{1}{\kappa}\ln Re_K - \frac{1}{\kappa}\ln k_{s_b}^+ - \frac{1}{\kappa}\ln c_r + B_{FR} \tag{12}$$

$$U^+ = \frac{1}{\kappa}\ln\left(\frac{y+y_0}{Re_K k_{s_b} c_r}\right) + B_{FR} \tag{13}$$

where c_r is the additional blockage term due to the presence of rough walls above the porous wall. From equation (13), k_s for porous-rough wall can be defined as

$$k_{s_{pr}} = Re_K k_{s_b} c_r \tag{14}$$

In order to fully isolate additional blockage effect from permeability, the analysis is conducted using cases with both matched Re_τ and Re_K. These cases are marked by asterisks ('*') in table 2, with the same coloured asterisk denotes matched Re_τ and Re_K). Four matched Re_K and Re_τ cases are identified for each set of **P**, **R**, and **PR** test surfaces. The criterion for matched Re_K is less than 10% difference between the Re_K calculated for **P** and **PR** surfaces.

Figure 9(a) shows the blockage effect k_s/Re_K for the porous and porous-rough walls, obtained via equation (9) and (14), respectively. Here, k_s for porous and porous-rough walls are obtained from the fitted ΔU^+ (figure 5e). As for Re_K, permeability K is obtained from Darcy flow measurements for the same type of porous wall (Esteban *et al.*, 2022), while U_τ is obtained from direct wall shear stress measurements. Figure 9(a) shows that the blockage effect (i.e. "roughness" size) decreases as permeability effect Re_K, as well as Re_τ, increases. It is noted that the rough walls on surfaces **PR1** and **PR2** increase the blockage effect from that of porous wall **P**. **PR1** has higher blockage than **PR2**, consistent with the higher C_f measured for both **PR1** and **R1** compared to that of **PR2** and **R2**, respectively.

Assuming that blockage effect (due to porous substrate) is the same for matched Re_K and thus k_{s_b} is the same both for porous and porous-rough surfaces, the additional blockage term c_r (due to rough walls above the porous wall) can be calculated via equation (14). Figure 9(b) shows c_r as a function of Re_τ, with $c_r = 1$ for the porous

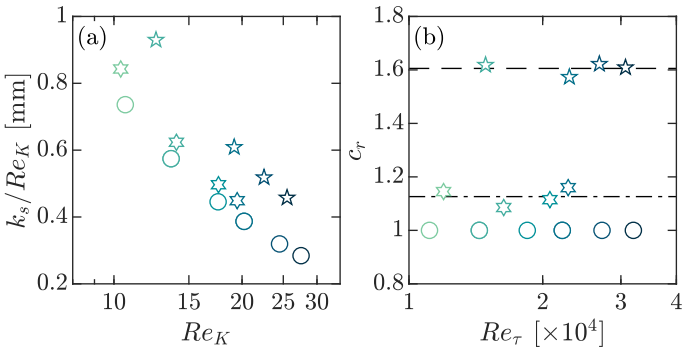

Figure 9: (a) Blockage effect k_s/Re_K and (b) additional roughness term c_r calculated for porous and porous-rough test surfaces. Colours show matched Re_τ and Re_K. Legends are shown in table 2.

wall **P**. For the porous-rough walls, an approximately constant magnitude of c_r is observed: $c_r = 1.61 \pm 1.52\%$ and $c_r = 1.13 \pm 3.30\%$ for **PR1** and **PR2**, respectively. It can be inferred that rough walls **R1** and **R2** increase blockage effect by 60% and 13%, respectively, irrespective of the Reynolds number. Considering that the blockage effect due to porous substrate (denoted by k_{s_b}) is the same for matched Re_K, it can be assumed that this additional blockage is solely due to the presence of **R1** and **R2** rough walls above the porous wall. Whether there is an empirical relation between c_r and the characteristic lengthscale of roughness (i.e. rough wall k_s) and whether it is possible to fully decouple the effect of roughness and permeability (i.e. whether it is possible to characterise a porous-rough wall given the information about its porous and rough wall components only) will be determined in the future.

4 Conclusions and future work

We conduct simultaneous streamwise velocity–wall-normal pressure fluctuation measurements of TBLs developing over porous, rough, and porous-rough wall combinations. Measurements are conducted over a high order of magnitude of Reynolds number ($11000 \leq Re_\tau \leq 32000$), with a set of matched Re_τ and permeability effect Re_K of each porous-rough combinations. Present results suggest that:

1. The increase in drag over porous, rough, and porous-rough walls is characterised by a downward shift in the logarithmic region ΔU^+ from that of smooth wall TBLs. Further analysis suggests that these surfaces can be characterised by k_s, and thus they can be characterised using the same framework as rough wall TBLs.

2. For the porous wall, k_s comprises of the effects of permeability and blockage from the porous substrate k_{s_b}. However, when rough walls are added above the porous wall, a constant increase of blockage effect by 61% and 13% is observed for two different type of rough walls, irrespective of Reynolds number for cases

with matched Re_τ and Re_K. This suggests the possibility of decoupling the effect of permeability and roughness. Empirical relations between this additional blockage and the characteristic lengthscale of roughness (i.e. rough wall k_s) will be determined in the future.

3. Examination of the 1-D premultiplied energy spectra of the streamwise velocity fluctuation over the porous-rough walls suggests a competing effect between porous and rough walls. Stronger influence of porous wall is observed near the wall, although one type of roughness (**R2**) noticeably affects the porous-rough wall in lower frequency range. The spectra is shown as a function of frequency of a given Fourier mode at present, with comparisons made at wall-normal locations corresponding with the same convection velocity. In the future, the viability of Taylor's hypothesis for time series to spatial conversion of the HWA signals should be examined. Analysis of coherence between turbulent structures and the wall-pressure fluctuations should also follow.

References

Breugem, W. P., Boersma, B. J. & Uittenbogaard, R. E. 2006 The influence of wall permeability on turbulent channel flow. *J. Fluid Mech.* **562**, 35–72.

Castro, I. P. 2007 Rough-wall boundary layers: mean flow universality. *J. Fluid Mech.* **585**, 469–485.

Chauhan, K. A., Monkewitz, P. A. & Nagib, H. M. 2009 Criteria for assessing experiments in zero pressure gradient boundary layers. *Fluid Dyn. Res.* **41**, 021404.

Coles, D. 1956 The law of the wake in the turbulent boundary layer. *J. Fluid Mech.* **1** (2), 191–226.

Efstathiou, Christoph & Luhar, Mitul 2018 Mean turbulence statistics in boundary layers over high-porosity foams. *J. Fluid Mech.* **841**, 351–379.

Esteban, L. B., Rodríguez-López, E., Ferreira, M. A. & Ganapathisubramani, B. 2022 Mean flow of turbulent boundary layers over porous substrates. *Phys. Rev. Fluids* (in print).

Fang, Hongwei, Han, Xu, He, Guojian & Dey, Subhasish 2018 Inflfluence of permeable beds on hydraulically macro-rough flow. *J. Fluid Mech.* **847**, 552–590.

Flack, K. A. & Schultz, M. P. 2010 Review of hydraulic roughness scales in the fully rough regime. *J. Fluids Eng.* **132** (4), 041203.

Hahn, Seonghyeon, Je, Jongdoo & Choi, Haecheon 2002 Direct numerical simulation of turbulent channel flow with permeable walls. *J. Fluid Mech.* **450**, 259–285.

Hama, F. R. 1954 Boundary-layer characteristics for rough and smooth surfaces. *Trans. SNAME* **62**, 333–351.

Hutchins, N., Nickels, T. B., Marusic, I. & Chong, M. S. 2009 Hot-wire spatial resolution issues in wall-bounded turbulence. *J. Fluid Mech.* **635**, 103–136.

Kong, F. & Schetz, J. 1982 Turbulent boundary layer over porous surfaces with different surface geometries. In *the 20th AIAA Aerospace Sciences Meeting*.

Ligrani, P. M. & Bradshaw, P. 1987 Subminiature hot-wire sensors: development and use. *J. Phys. E: Sci. Instrum.* **20**, 323–332.

Manes, C., Poggi, D. & Ridolfi, L. 2011 Turbulent boundary layers over permeable walls: scaling and near-wall structure. *J. Fluid Mech.* **687**, 141–170.

Manes, Costantino, Pokrajac, Dubravka, McEwan, Ian & Nikora, Vladimir 2009 Turbulence structure of open channel flows over permeable and impermeable beds: A comparative study. *Phys. Fluids* **21**, 125109.

Marusic, I., Chauhan, K. A., Kulandaivelu, V. & Hutchins, N. 2015 Evolution of zero-pressure-gradient boundary layers from different tripping conditions. *J. Fluid Mech.* **783**, 379–411.

Monty, J. P., Dogan, E., Hanson, R., Scardino, A. J., Ganapathisubramani, B. & Hutchins, N. 2016 An assessment of the ship drag penalty arising from light calcareous tubeworm fouling. *Biofouling* **32** (4), 451–464.

Nikuradse, J. 1933 Strömungsgesetze in rauhen rohren. *VDI Forschungsheft* **361**, English translation: 1950 Laws of flow in rough pipes. *NACA Tech. Mem.* **1292**.

Rodríguez-López, E., Bruce, P. J. K. & Buxton, O. R. H. 2015 A robust post-processing method to determine skin friction in turbulent boundary layers from the velocity profile. *Exp. Fluids* **56**, 68.

Rosti, Marco E., Cortelezzi, Luca & Quadrio, Maurizio 2015 Direct numerical simulation of turbulent channel flow over porous walls. *J. Fluid Mech.* **784**, 396–442.

Shimizu, Y., Tsujimoto, T. & Nakagawa, H. 1990 Experiment and macroscopic modelling of flow in highly permeable porous medium under free-surface flow. *J. Hydrosci. Hydraul. Eng.* **8** (1), 69–78.

Suga, K., Matsumura, Y., Ashitaka, Y., Tominaga, S. & Kaneda, M. 2010 Effects of wall permeability on turbulence. *Int. J. Heat Fluid Flow* **31**, 974–984.

Zagni, Anthony F. E. & Smith, Kenneth V. H. 1976 Channel flow over permeable beds of graded spheres. *J. Hydraul. Div.* **102** (2), 207–222.

Zippe, Hans J. & Graf, Walter H. 1983 Turbulent boundary-layer flow over permeable and non-permeable rough surfaces. *J. Hydraul. Res.* **21** (1), 51–65.